Improving ATMS Imagery Visualization Using Limb Correction and AI Resolution Enhancement

Xingming Liang, Lihang Zhou, Mitch Goldberg, Satya Kalluri, Christopher Grassotti, Ninghai Sun, Banghua Yan, Hu Yang, Lin Lin, and Quanhua Liu

***Abstract*—The advanced technology microwave sounder (ATMS) is an important satellite instrument that provides vital data on atmosphere temperature and moisture for weather forecasting and climate research, and helps us plan for extreme weather. However, its coarse resolution and angular dependence have long been a challenge for improving image visualization. This article proposes a method to enhance the imagery visualization for ATMS, combining limb correction (LC) with artificial intelligence (AI) resolution enhancement (RE). Measurement data from the ATMS onboard NOAA-20 were utilized to train the LC method, which were then validated using newly acquired NOAA-21 ATMS data. The AI RE was performed using enhanced super-resolution generative adversarial networks, which increased the pixel resolution by a factor of four. The high-resolution (HR) Advanced Microwave Scanning Radiometer 2 data served as a reference to initially and quantitatively evaluate the RE method. The combined method of LC and AI RE produced an angular-dependence-free and HR ATMS image, resulting in a significant improvement in image visualization, including surface and atmosphere information, and allows for clear identification of severe weather events. For the swift identification and analysis of tropical cyclones in the upcoming season, as of this writing, this proposed method has been routinely employed to produce high-quality global ATMS images, and these images are showcased and tested in the NOAA internal HR imagery visualization system—JSTAR Mapper. Moreover, concentrated efforts are being made to further enhance these images in preparation for an official release.**

***Index Terms*—Advanced technology microwave sounder (ATMS), convolutional neural network (CNN), enhanced super-resolution generative adversarial networks (ESRGAN), generative adversarial network (GAN), image visualization, limb correction (LC), weather event.**

Manuscript received 12 August 2023; revised 16 November 2023 and 18 December 2023; accepted 2 January 2024. Date of publication 18 January 2024; date of current version 12 February 2024. This work was supported by the National Oceanic and Atmospheric Administration under Grant NA19NES4320002 to Cooperative Institute for Satellite Earth System Studies at the Earth System Science Interdisciplinary Center of University of Maryland. *(Corresponding author: Xingming Liang.)*

Xingming Liang, Christopher Grassotti, Hu Yang, and Lin Lin are with the ESSIC, University of Maryland, College Park, MD 20740 USA (e-mail: xingming.liang@noaa.gov; christopher.grassotti@noaa.gov; huyang@umd.edu; lin.lin@noaa.gov).

Lihang Zhou, Satya Kalluri, Banghua Yan, and Quanhua Liu are with the Center for Satellite Applications and Research, NESDIS, NOAA, College Park, MD 20740 USA (e-mail: lihang.zhou@noaa.gov; satya.kalluri@noaa.gov; banghua.yan@noaa.gov; quanhua.liu@noaa.gov).

Mitch Goldberg is with the NOAA Center for Earth System Sciences and Remote Sensing Technologies, New York, NY 10031 USA (e-mail: mitch.goldberg@noaa.gov).

Ninghai Sun is with the Global Science and Technology, Inc., Greenbelt, MD 20770 USA (e-mail: ninghai.sun@noaa.gov).

Digital Object Identifier 10.1109/JSTARS.2024.3354103

I. Introduction

THE advanced technology microwave sounder (ATMS) [1] produces imagery products from sensor data records (SDRs) that provide a preliminary view of surface and atmospheric information. This enables users to quickly and directly identify and analyze extreme weather events, such as tropical cyclones (TCs), and respond to disasters in a timely manner. However, there are two limitations of ATMS imagery for this application that hinder the usefulness of surface and atmospheric information and the clear identification of extreme weather events. First, the measurement data from ATMS SDR products are highly dependent on the sensor scan angle [1], [2], which is a characteristic of the cross-track microwave sensor of ATMS. This angle dependence reduces the accuracy of the view of surface or atmospheric information and identification of weather events from ATMS imagery products, as the atmosphere's optical path length varies from the nadir to the swath edge. Second, most microwave sensors have low spatial resolutions. For example, the nadir spatial resolution of ATMS is 75 km for channels 1–2, 32 km for channels 3–16, and 16 km for channels 17–22, which is lower than visible and infrared sensors. The resolution is further decreased as one moves toward the swath edge (off-nadir). The low resolution (LR) of microwave channels significantly limits the depiction of surface and atmospheric information and the clear identification of extreme weather events, especially at the swath edge.

Efforts to correct the scan angle dependence of cross-track microwave sensors, also known as limb correction (LC), have been extensively researched at NOAA. Wark [3] first introduced the linear regression method for adjusting the limb effect at each scan angle, and Goldberg et al. [4] further developed the LC method and applied it to the advanced microwave sounding unit (AMSU). Liu and Weng [5] validated Goldberg's LC method using AMSU on NOAA-16 and NOAA-18.

Zhang et al. [6] applied the algorithm to ATMS onboard the Suomi National Polar-Orbiting Partnership (S-NPP), and Tian et al. [7] used the method on the Microwave Temperature Sounder 2 onboard FengYun 3C. These LC efforts for microwave sensors have minimized the scan angle dependence of the sensor measurements and improved the microwave sensor imagery. Meanwhile, efforts have also been made at NOAA to improve the capability of microwave sensor imagery visualization for accurately capturing weather events. Yan et al. [8] filled gaps in ATMS SDR data in low latitude regions to help visually observe

realistic warm core structures of a hurricane system. Zhou et al. [9] presented the atmospheric features of the Hunga Tonga volcano eruption using ATMS, together with three other advanced sensors onboard the Joint Polar Satellite System (JPSS) satellites. However, the lack of fine resolution footprints for cross-track microwave sensors still prevents accurate capturing of surface and atmosphere information and weather events, particularly when the important information or weather event is located at coarser footprints close to the swath edge.

NOAA-20, formerly known as JPSS-1, was launched in November 2017, and operates in the same orbit as the S-NPP satellite, with a lead time of approximately 50 min. NOAA-20 ATMS has the same channel set, polarizations, scan geometry, and calibration approach as the S-NPP ATMS and is currently operational at NOAA [10]. It is valuable to develop and validate the limb adjustment algorithm for NOAA-20 ATMS in order to improve NOAA's imagery products and Environmental Data Record (EDR) products. The recently launched NOAA-21, also carrying the ATMS sensor, will be operational at NOAA as part of the JPSS satellites series. This article adopts a similar linear regression method as previous article, but with slightly altered parameterization, to limb-correct NOAA-20 ATMS SDR data. The newly acquired NOAA-21 ATMS data will be utilized to validate the LC algorithm through a comparison of measurements from NOAA-20 and NOAA-21.

Artificial intelligence (AI) and deep learning (DL) are rapidly evolving fields that have had a significant impact on numerous areas of science and engineering. DL, in particular, has become one of the most widely used AI methods. Its applications in remote sensing and numerical weather prediction are currently being investigated [11], [12], [13], [14], [15], [16]. The remote sensing image processing using a state-of-art convolutional neural network (CNN) [17], [18], [19], [20], [21], [22] method has also become popular [23], [24]. The recent advancements in AI have led to the development of various methods for generating super-resolution (SR) images from LR images using CNN methods. Single image SR is a fundamental image processing task that aims to enhance image resolution by recovering high-resolution (HR) images from LR images. Traditional resolution-enhancement methods, such as bicubic interpolation and Lanczos filtering [25], have limitations in terms of generating high-quality images with fine texture details. To overcome these limitations, researchers have developed various CNN-based SR models. The first SR method was SR CNN [26], which used only two simple convoluted layers but opened the door for later evolution of SR model development. It was soon discovered that a very deep CNN is good for the SR method and a very deep super-resolution method [27] was proposed in 2015. With the emergence of state-of-the-art generative adversarial networks (GAN) [17], new SR methods, such as the super-resolution generative adversarial networks (SRGAN) [28] and enhanced super-resolution generative adversarial networks (ESRGAN) [29], were developed to improve SR image at larger upscaling factors and recover finer texture details in images. While this is a brief summary of the evolution of SR technique, there have been many other SR methods developed in recent years. ESRGANs, in particular, have been praised for their high level of detail and natural appearance, making them well-suited for applications in computer graphics, video compression, image processing, and remote sensing. One area of this article is exploring the enhancement of spatial resolution in ATMS imagery using ESRGAN. This seminal work has the capability to generate realistic textures from a single image that has undergone resolution enhancement (RE).

The rest of this article is organized as follows. Section II outlines the LC algorithm, RE method, and data used for both methods. Section III demonstrates and evaluates the results. Specifically, the NOAA-20 LC algorithm is examined by newly acquired NOAA-21 data, and its compatibility is checked by S-NPP. In addition, the accuracy of the generated RE image is initially assessed using HR Advanced Microwave Scanning Radiometer 2 (AMSR2) data. Section IV discusses the merits and drawbacks of applying ESRGAN to ATMS imagery. Finally, Section V concludes this article.

II. Methodology and Data

The LC and RE algorithms were both utilized in this article and processed sequentially to generate combined LC and RE images. In this section, the algorithms will be described individually along with the corresponding data used.

A. Limb Correction for ATMS NOAA20

As described in the previous section, NOAA-20 ATMS has the same channel set, polarizations, scan geometry, and calibration approach as the S-NPP ATMS. However, they have slightly different noise equivalent to differential temperature (NEDT, https://www.star.nesdis.noaa.gov/jpss/ATMS.php).

Despite operating in nearly the same orbit, there is 50-min difference between the two satellites. In addition, the coefficients generated in previous articles may have become outdated and may need to be upgraded for recent brightness temperature (BT) adjustments. Thus, it is necessary to redevelop the LC algorithm to adjust NOAA-20 ATMS BTs and reduce its scan angle dependence.

The scan angle dependencies of ATMS measurements are caused by the satellite limb effect, which results from an increase in the atmosphere optical path between the satellite and the earth surface as the satellite zenith angle (SZA) increases, while the sensor scans from nadir to swath end. The objective of the LC method is to adjust the off-nadir BT to the nadir-like BT for each scan angle using a linear regression method with selected neighboring channels. It is based on an empirical hypothesis that the limb effect for a target channel can be eliminated or minimized by a linear combination of its neighboring channels and itself [3], [4]. This can be expressed as follows:

$$\overline{Tb}_{m,j,\ \text{nadir}} = \overline{Tb}_{m,i} + \sum_{mk} \alpha_{mk,i} * \left(\overline{Tb}_{mk,i,j} - \overline{Tb}_{mk,i}\right) \tag{1}$$

where $\overline{Tb}_{m,j,\ \text{nadir}}$ is the mean BT at channel m at the ATMS nadir field of views (FOVs), specifically positions 47 and 48. The index j represents each latitude bin group, where each latitude group represents the angular variation of a single metrological

TABLE I
MEAN BIASES AND SDS BETWEEN THE LC BTS AND NADIR BTS IN NOAA-20 ATMS 22 BANDS AND 7 FOVS FOR TRAINING DATASET

	Mean							SD						
CH \ FOV	1	16	32	48	64	80	96	1	16	32	48	64	80	96
1	−0.20	−0.09	−0.02	0.00	−0.02	−0.11	−0.23	2.461	0.69	0.282	0.09	0.265	0.551	2.493
2	−0.13	−0.08	−0.02	0.00	−0.02	−0.10	−0.15	2.391	0.703	0.307	0.097	0.311	0.639	2.535
3	0.11	0.03	0.00	0.00	0.00	0.02	0.13	1.172	0.475	0.189	0.039	0.157	0.408	1.273
4	0.05	0.02	0.00	0.00	0.00	0.00	0.06	0.701	0.286	0.112	0.024	0.093	0.243	0.766
5	0.02	0.01	0.00	0.00	0.00	0.00	0.02	0.29	0.094	0.039	0.01	0.028	0.083	0.319
6	0.02	0.00	0.00	0.00	0.00	0.00	0.01	0.134	0.032	0.014	0.005	0.016	0.038	0.13
7	−0.01	0.00	0.00	0.00	0.00	0.00	−0.01	0.037	0.015	0.012	0.003	0.008	0.017	0.045
8	0.00	0.00	0.00	0.00	0.00	0.00	−0.01	0.022	0.009	0.007	0.003	0.007	0.012	0.033
9	−0.02	0.00	0.00	0.00	0.00	0.00	−0.02	0.101	0.016	0.009	0.003	0.008	0.014	0.093
10	0.01	0.01	0.00	0.00	0.00	0.00	0.01	0.102	0.04	0.012	0.003	0.01	0.029	0.107
11	0.00	0.00	0.00	0.00	0.00	0.00	0.00	0.032	0.012	0.009	0.005	0.008	0.011	0.017
12	0.01	0.01	0.00	0.00	0.00	0.00	0.00	0.031	0.015	0.011	0.005	0.009	0.015	0.026
13	0.02	0.01	0.01	0.00	0.00	0.00	−0.01	0.05	0.031	0.017	0.006	0.014	0.036	0.058
14	0.02	0.01	0.01	0.00	−0.01	0.00	−0.03	0.065	0.044	0.023	0.007	0.019	0.044	0.096
15	0.01	0.01	0.01	0.00	−0.01	−0.01	−0.02	0.069	0.044	0.028	0.009	0.026	0.064	0.146
16	0.04	0.02	0.00	0.00	0.00	0.00	0.06	0.791	0.518	0.263	0.042	0.233	0.414	0.84
17	−0.05	−0.02	−0.02	0.00	−0.01	−0.03	−0.03	0.382	0.264	0.158	0.017	0.152	0.198	0.436
18	−0.03	−0.01	0.00	0.00	0.00	−0.01	−0.03	0.239	0.182	0.114	0.015	0.114	0.158	0.273
19	−0.03	−0.01	0.00	0.00	0.00	−0.01	−0.03	0.277	0.15	0.096	0.013	0.097	0.125	0.286
20	−0.03	−0.01	0.00	0.00	0.00	−0.01	−0.03	0.171	0.13	0.087	0.012	0.086	0.11	0.212
21	−0.02	−0.01	0.00	0.00	0.01	0.00	−0.02	0.139	0.116	0.083	0.011	0.08	0.103	0.177
22	0.00	−0.01	0.00	0.00	0.00	−0.01	0.00	0.147	0.114	0.084	0.011	0.078	0.106	0.163

condition, such as temperature, humility, ozone, and clouds. Unlike previous articles that binned the data into 2° latitude bands, this article bins the train data into 1° to provide more detailed metrological conditions and bring more cases to the model training, which can improve the model ability to capture the underlying relationship between variables and help in estimating the regression coefficients more accurately. Consequently, this update in latitude binning makes it possible to improve the LC algorithm. $\overline{Tb}_{m,i}$ represents an average BT at FOV *i* and channel *m*. $\overline{Tb}_{mk,i,j}$ is the mean BT for selected channel *mk* and FOV *i* at the latitude bin position *j*, and $\overline{Tb}_{mk,i}$ is the corresponding average BT in all latitude bins. $\alpha_{mk,i}$ are the coefficients to be determined. The adjacent channel selection process for a target channel can be found in previous article [6]. The coefficients can be obtained by a simple linear regression algorithm fed by a precollected training dataset. Once the $\alpha_{mk,i}$ are obtained, the LC BTs ($Tb\_LC_{m,j,i}$) can be calculated using right terms of (1) and replacing the $\overline{Tb}_{mk,i,j}$ with original SDR measurements ($Tb_{mk,i,j}$) as follows:

$$Tb\_\mathrm{LC}_{m,j,i} = \overline{Tb}_{m,i} + \sum_{mk} \alpha_{mk,i} * \left(Tb_{mk,i,j} - \overline{Tb}_{mk,i}\right). \tag{2}$$

This article used six months of NOAA-20 ATMS SDR data from June 1, 2021 to December 1, 2021, which were accumulated and grouped into 1° latitude bands to generate LC coefficients for each channel and each FOV position. The data were further separated into land and sea groups to avoid potential biases from different surfaces, especially for surface-sensitive window channels, due to the significant surface emissivity difference between land and sea. A newly developed 0.05° horizontal-resolution global surface type model used in the NOAA Microwave Integrated Retrieval System (https://www.star.nesdis.noaa.gov/mirs/) was employed to separate the dataset to land and sea groups. To further validate the accuracy of the generated coefficients, the mean biases between the LC-adjusted BTs and nadir BTs for training dataset and corresponding standard deviations (SDs) were calculated. Table I shows these mean biases and SDs across all 22 channels and 7 FOV positions in ocean domain between latitudes of −60° and +60°. Higher latitudes were excluded from the error analysis as they introduce more noise due to snow and ice, and increase SDs for window bands.

The small biases and SDs suggest that the LC adjustment works well and the uncertainties from cloud and surface emissivity are almost minimized or eliminated after averaging six months data. Most biases and SDs are smaller or comparable to NOAA-20 ATMS NEΔTs, except for window bands at swath end, which show uncertainties up to 2.5 K, mainly due to the effect of complex surface emissivity. The angular dependences are observed for both mean biases and SDs, but SDs are more pronounced, attributed to the increase in atmosphere optical path from nadir to swath end. Certainly, when applying the LC algorithm to individual ATMS measurements, both mean biases and SDs in term of nadir BTs are expected to be larger than those for training dataset, due to the contribution from the specific metrological condition and surface state in each measurement. However, the angular dependences are considered

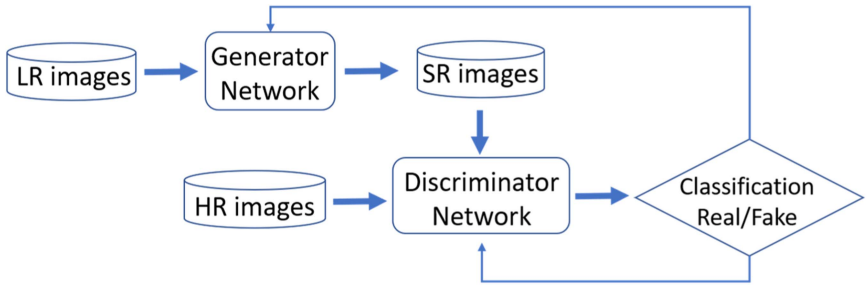

Fig. 1. Flowchart of ESRGAN.

to be eliminated or minimized after LC adjustment. Further discussion will be in the next section.

The mean biases and SDs for land (no shown) were found to be similar to those for the ocean, except that the SDs are slightly larger for window bands. This is because that the surface emissivity differs for different surface type and atmospheric optical properties for land are more complicated and nonuniform than those for the ocean. Nevertheless, the patterns of the biases and SDs in term of ATMS channels and FOV positions, including angular dependence, were similar to those for the ocean. The snow and ice surface produced even larger biases and SDs as the surface emissivity varies more rapidly with frequency under snow and ice conditions. Moreover, most ice data is located in dry-air polar areas, making the effect on LC from the surface emissivity is more significant. However, for high-peaking sounding channels, such as band 12–15, which are not sensitive to atmosphere conditions of surface and low troposphere, the LC adjustment can still work for ice surfaces. In this article, we focused on LC adjustment for land and ocean surfaces and left the option of LC for ice in the algorithm for future investigation.

B. Overview of ESRGAN

ESRGAN [29] is a DL algorithm designed to generate SR image, representing an upgraded version of its "sister" model, SRGAN. Its core architecture is based on a cutting-edge neural network known as GAN, which consists of two independent learning networks: the generator and the discriminator. The generator is trained to create SR images, while the discriminator attempts to classify these SR images as either real or fake. Both networks are very deep CNNs and are trained using a large dataset of LR and HR image pairs. The objective of the ESRGAN is to produce SR images that are as close to nature HR images as possible from LR inputs, as demonstrated in Fig. 1. Initially, the LR image is input into the generator network to generate an HR version, known as SR image. This generated image, along with the original HR image, is then fed into the discriminator network, which is responsible for distinguishing between real and fake images based on the GAN loss function. During backpropagation, the GAN loss function is utilized to update model's weights and biases. The generator network learns to generate SR images that are as realistic as possible, with the aim of deceiving the discriminator network, which is trained to distinguish real and fake images. Together, both models work collaboratively to make ESRGAN capable of generating SR images that are indistinguishable from their original HR counterparts.

A vital advantage of SRGAN and ESRGAN is the incorporation of the perceptual loss function [28] in the generator model. This is in addition to the common pixelwise mean square error (MSE) loss used in earlier SR image models as follows:

$$L_G = L_{\text{percep}} + \lambda L_G^{Ra} + \eta L_1. \tag{3}$$

Here, L_1 is the content loss, which is the well-known pixelwise MSE-based loss. L_{percep} is the perceptual loss, and remaining term is the adversarial loss [30]. The coefficients λ and η balance different loss terms.

In SRGAN, the perceptual loss is calculated using the after-activation feature map of a pretrained, very deep CNN architecture developed by visual geometry group, the so-called VGG network [31]. By incorporating the perceptual loss into generator network, the generated SR images recover finer texture details of the original HR images, compared to pixelwise MSE loss, which often lacks high-frequency content and results in overly smooth textures in the generated SR images. ESRGAN further improves the perceptual loss by using features before activation, which can lead to better brightness consistency and texture recovery.

The common adversarial loss used in SRGAN is defined based on the probability that the generated SR image is a natural HR image, as shown in (4). It was updated to the relativistic generator loss in ESRGAN as follows:

$$L_G^{SR} = -\mathbb{E}_{x_f}\left[\log\left(D\left(x_f\right)\right)\right] \tag{4}$$

$$L_G^{Ra} = -\mathbb{E}_{x_r}\left[\log\left(1 - D_{Ra}\left(x_r,\, x_f\right)\right)\right] - \mathbb{E}_{x_f}\left[\log\left(D_{Ra}\left(x_f, x_r\right)\right)\right]. \tag{5}$$

In these equations, x_r and x_f represent the real HR image and the generated fake image, respectively. $D(x_f)$ is the probability that the reconstructed SR image x_f is real and natural. This probability needs to be maximized to generate a realistic HR image. So L_G^{SR} needs to be minimized. However, the relativistic loss aims to predict the probability that a real image is relatively more realistic than a fake one, as shown in (5), which aids in learning shaper edges and more detailed textures.

Furthermore, ESRGAN removes batch normalization [14], used in SRGAN, to further minimize artifacts in the generated

image and employs a residual-in-residual dense block instead of the original residual block to improve training stability. All these advantages enable ESRGAN to effectively enhance image resolution at larger upscaling factors.

C. ATMS Resolution Enhancement With ESRGAN

There are several challenges in applying ESRGAN to ATMS imagery. One challenge is that ESRGAN requires both LR and HR image pairs for model training. In the case of ATMS, HR reference data are lacking, and using the original ATMS imagery as HR imagery and resolution-lowered images as LR imagery is not effective as the coarse resolution original ATMS images have been blurred and will lose much high-frequency information, particularly in the off-nadir region. In addition, most current SR methods are designed for single images, making it difficult to enhance the resolution for the multiple ATMS channels simultaneously.

To overcome these challenges, the high-quality image set, DIVerse 2K (DIV2K, https://data.vision.ee.ethz.ch/cvl/DIV2K/) was used to train the model in this article. The DIV2K dataset contains 1000 2K resolution high-quality images with different scenes and was split into 800 for training, 100 for validation, and 100 for testing. It was collected from Internet for the New Trends in Image Restoration and Enhancement (NTIRE) 2017 [32] and NTIRE2018 SR challenges to encourage research in image SR with more realistic degradation. As a result, a four-times RE model pretrained with the DIV2K dataset was used to generate ATMS images for the subsequent evaluation. While considering a larger upscaling factor is possible, our offline tests suggest that it may not effectively recover detailed texture and information of LR, off-nadir pixels.

ATMS SDR data are used as inputs for the RE model to generate HR images. Ideally, the RE model requires that the size of each pixel in the input image be identical, as the images in the DIV2K dataset used for model training are composed of same-size pixels. Consequently, it would seem more reasonable to use a gridded ATMS image as an input for the RE model to generate HR image. However, if ATMS SDR data are gridded, the resolution of the input images would be significantly reduced and the gridded pixel will be inconsistent with original one, making the benefits of to enhancing gridded ATMS data far less impactful than using ATMS SDR data directly. Moreover, compared to SDR data, the use of gridded data degrades surface and atmosphere information, particularly for the severe weather events. Therefore, the original resolution SDR data are initially selected as the model input. Although the resolution of ATMS SDR data changes from nadir to swath edge, it does not affect the four-fold RE after RE processing, excepted that the generated images maintain unequal resolution across the scan swath. For instance, an ATMS image that originally has a resolution of 16 km at the nadir but 60 km at the swath edge would be refined to 4 km at the nadir and 15 km at the swath edge after undergoing RE processing. Therefore, after RE processing, the ATMS nadir spatial resolution will be improved to 18.75 km for channels 1 and 2, 8 km for channels 3–16, and 4 km for channels 17–22, from their original resolutions described in Section I.

Since the DIV2K dataset comprises photos with a 256 RGB colors scale, the BTs from ATMS SDR data should be normalized and convert to photo scale before being input into RE model. A Min–Max scaling technique is used as follows:

$$X_{\text{norm}} = \frac{X - X_{\text{min}}}{X_{\text{max}} - X_{\text{min}}} * 255. \tag{6}$$

Here, X_{max} and X_{min} are maximum and minimum BTs of the input SDR data, respectively. As the BT range are approximately 100 to 350 K for all ATMS bands, which is nearly the same order of magnitude as the DIV2K image scale, the error resulting from this conversion can be ignored.

The RE model was designed to accommodate the input of multiple SDR granule BTs. Each granule contains 12 sample lines and 96 FOVs. To enhanced processing efficiency, BTs from several contiguous ATMS SDR granules are combined and fed into the RE model after being normalized using (6). As a result, after RE processing, a $4 \times$ lines by 4×96 SR image is generated, in which each 4×4 pixel block is reconstructed from one SDR pixel. Subsequently the produced data will be inverse-normalized and converted back to BTs as follows:

$$X = X_{\text{norm}} * (X_{\text{max}} - X_{\text{min}}) / 255 + X_{\text{min}} \tag{7}$$

D. Combination of Limb Correction and Resolution Enhancement

Given the newly generated LC coefficients and a well-trained RE model, both methods can be combined to process ATMS images. Fig. 2 presents the flowchart of ATMS image processing that combines both methods. First, the ATMS SDR data are input into the LC module to generate the LC image, and then the LC image is input into the RE module to generate high-quality LC and RE images, which are used to accurately view the surface and atmospheric state and clearly identify extreme weather events. Another option is to perform the RE algorithm first to generate the RE image and then conduct the limb adjustment to produce RE and LC images. However, the latter procedure is more complex and time-consuming as the LC processing requires the use of multiple RE images of selected channels to generate the LC image for a single target channel. This alternative approach will serve as an option to supplement the primary processing strategy.

III. Results and Evaluation

The generated NOAA-20 LC coefficients and well-trained RE model were used to generate LC and RE images, and is further evaluated in this section.

A. Limb-Correction BTs

Fig. 3 presents the global maps of BTs before and after limb adjustment for NOAA-20 ATMS in channels 1, 6, and 18, which cover the window, temperature, and water vapor sounding channels. The corresponding FOV position dependencies of the BTs are shown in the right panels. The clear scan dependence in the original SDR BTs [Fig. 3(a), (b), and (c)] are significantly reduced or eliminated after LC [Fig. 3(d), (e), and (f)], resulting

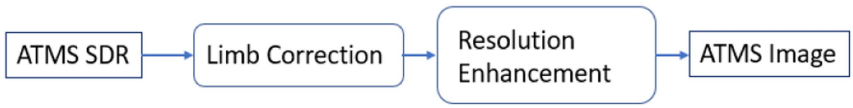

Fig. 2. Flowchart of ATMS image processing.

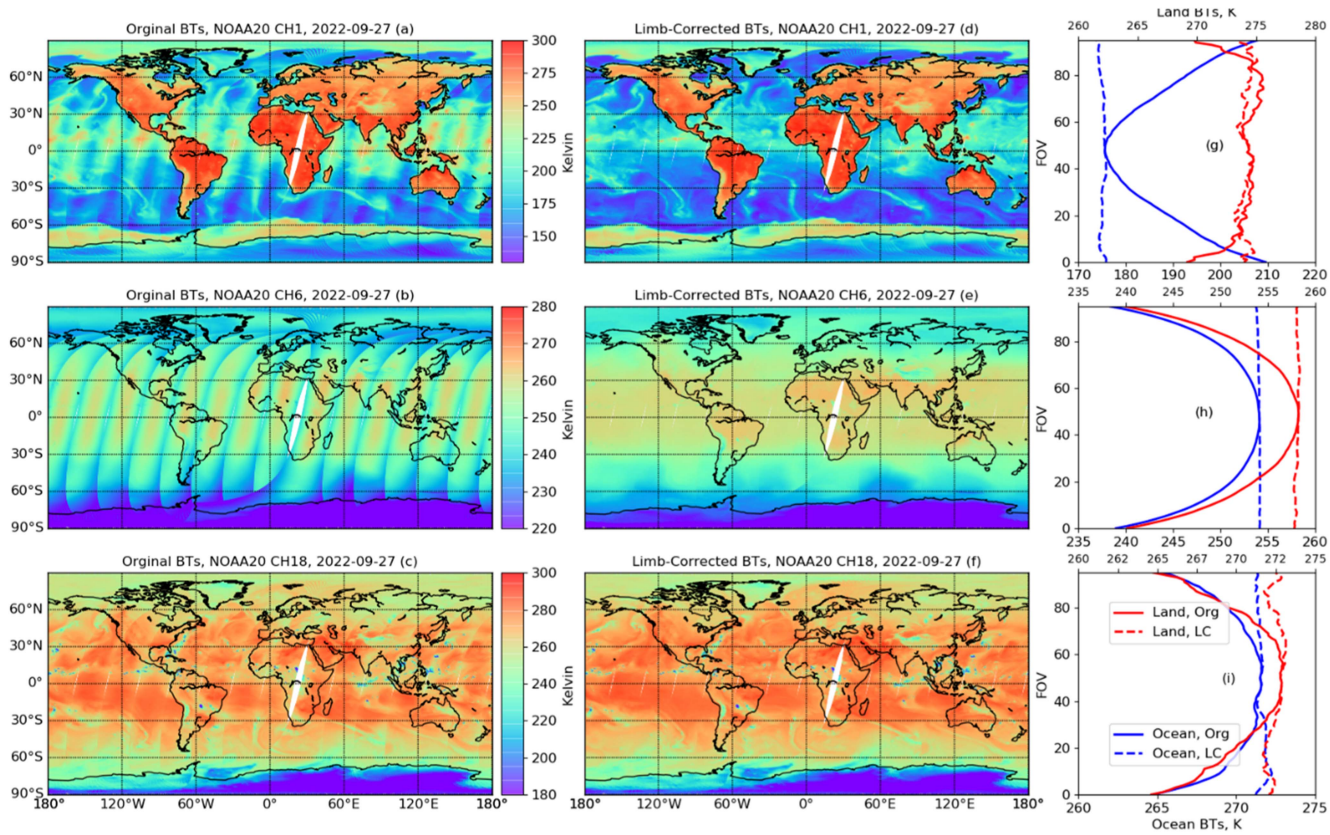

Fig. 3. Global maps of NOAA-20 ATMS brightness temperatures without (a), (b), (c) and with (d), (e), (f) limb correction for channel 1, 6, and 18 in 09/27/2022 and corresponding FOV position dependencies (g), (h), and (i). In panels (g), (h), and (i), the lower (upper) x-axis values refer to the ocean (land) curves.

in a more natural and smooth distribution of global BTs. As a result, the global atmospheric and surface features are more pronounced after limb adjustment.

The FOV position dependencies of the BTs were obtained by averaging the BTs in each FOV position and dividing into land and ocean in a range of [−60°, 60°] latitude to avoid possible biases from snow or ice. For the window channel 1, the FOV position dependencies, up to 15 K from nadir to the swath end for the ocean domain, were corrected to nearly flat, and all off-nadir BTs were adjusted to the nadir value. Although the angle dependence for land is not pronounced and the limb-corrected BTs are somewhat noisy, they still provide a near free-angular-dependence across the entire swath. After LC adjustment, the BTs over ocean are about 100 K smaller than over land, mainly due to low sea surface emissivity for window channels, although the surface emissivity may slightly increase away from nadir, which is attributed to the polarization effect in channel 1 [4]. There is a 15–20 K dependence in the temperature sounding channel 6, but it becomes completely flat in the entire FOV range for both land and ocean after LC processing, indicating that the LC works well for the temperature sounding channels as they are seldom affected by surface state. For the humidity channel 18, the BTs are slightly noisy after LC processing, but still result in a near free-angle-dependence and the corrected BTs are up to 7 K for both land and ocean. The LC for the other ATMS channels is comparable to the three channels presented. Overall, the initial analysis indicates that LC works well for NOAA-20, and most of off-nadir observations are adjusted to the nadir value.

B. NOAA-20 LC BTs Evaluation With NOAA-21

In this section, we evaluated the NOAA-20 limb-corrected BTs using the data from the recently launched NOAA-21 ATMS. The NOAA-21 satellite, formerly known as JPSS-2, was successfully launched on November 10, 2022 and will provide operational continuity for satellite-based observations and products for several environmental satellite programs. Shortly after launch, the orbit of NOAA-21 was gradually adjusted such that

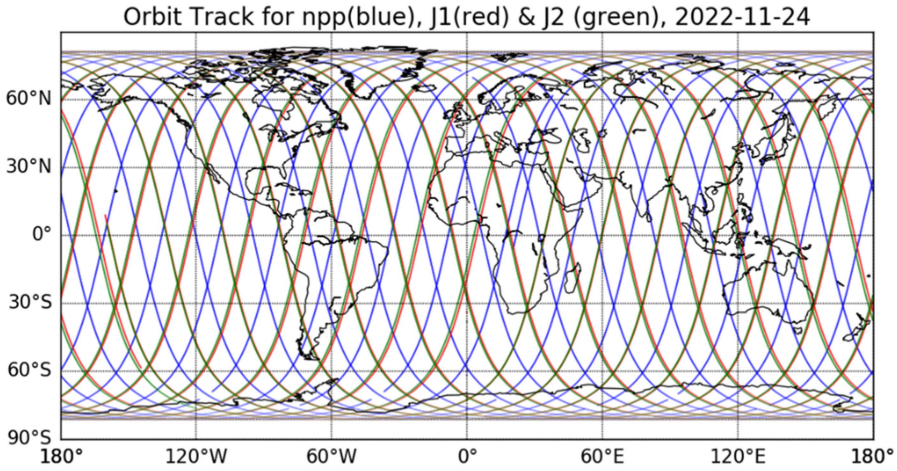

Fig. 4. Orbit tracks for S-NPP, NOAA-20, and NOAA-21 on 11/24/2022. NOAA-20 and NOAA-21 orbits are nearly coincident.

it would eventually fly roughly 50 min ahead of the NOAA-20 satellite. This provided an opportunity to evaluate the LC performance on NOAA-20 using NOAA-21 as a reference when the two satellites orbits were nearly collocated in space and time during the NOAA-21 orbit adjustment.

Fig. 4 illustrates that the close proximity between NOAA-21 and NOAA-20 orbits on November 24, 2022, which allowed for the comparison of the off-nadir observations of NOAA-20 ATMS with the nadir observations of NOAA-21 ATMS.

ATMS SDR data from November 24–25, 2022 were selected and approximately 60 000-pixel pairs between NOAA-20 and nadir observations of NOAA-21 were collected each day using a $\pm$5-min time collocation window and a 10-km spatial collocation window. The difference between the original and LC BTs, minus the NOAA-21 BTs, as functions of the FOV positions for eight ATMS channels is shown in Fig. 5, along with the corresponding distribution of pair pixels. As the two satellites are in close proximity, the collocated pixels only include the FOV scan positions 39 to 56. An offline test showed that the range of collocated FOV positions did not change significantly even if the time window was expanded to $\pm$10-min and the spatial window was expanded to 30 km, although the number of pair pixels increased significantly.

The distribution of collocated pixels (bottom right panel of Fig. 5) was concentrated at nadir on November 25, 2022, but was reversed on November 24, 2022, which suggests that the orbit of NOAA-21 was closer to NOAA-20 on November 25, 2022. For channels 1, 2, 7, 8, and 16, the difference in BTs showed a clear FOV position dependence before NOAA-20 LC adjustment, but were close to flat with some slight noise after the LC adjustment. The mean biases between the BTs of NOAA-20 LC adjustment and NOAA-21 nadir are not zero and the values are depended on the channels. These remaining biases will be further investigated after the NOAA-21 SDR is well calibrated and reprocessed. Temperature sounding channels 7 and 8 demonstrated the best LC adjustment with the least noise among the eight analyzed channels. Channel 11 also exhibited a noticeably reduced angle dependence after LC, although with significant instability and noise. Similarly, channels 18 and 21 displayed more oscillation along with the FOV position, which could be partially attributed to the differences in atmosphere water vapor content between the matchup pixels. This is because the collocation was not conducted at the exact same time and location. Nonetheless, we observed that the angle dependencies were almost completely removed or reduced after LC adjustment for these channels.

C. Applying NOAA-20 Limb Correction for NPP

In this section, we assess the compatibility of the LC coefficients obtained from the NOAA-20 with other satellites, such as S-NPP and NOAA-21. Although there are some differences in the NEDTs of the ATMS channels between the different satellites, these differences are generally smaller than the amplitude of the angle-dependent BTs as showed in Fig. 3. Hence, it is possible to use NOAA-20 coefficients to limb adjust S-NPP and NOAA-21 ATMS measurements. To test the compatibility of the NOAA-20 LC coefficients, we calculated LC BTs for S-NPP using the NOAA-20 coefficients, and show the results in Fig. 6. Both global distribution and angle dependencies after LC adjustment for S-NPP showed comparable patterns with Fig. 3 for all three channels, indicating that the NOAA-20 LC coefficients still work well for S-NPP. In an offline test, we also tested NOAA-20 LC coefficients applied to NOAA-21 and found that the adjusted BTs reduced the angle dependence, which is similar to Figs. 3 and 6, further indicating that the NOAA-20 coefficients can be applied to its sister satellites. The reason for this compatibility is that the scan angle dependencies for the ATMS can reach 10–20 K for most channels, as seen in Figs. 3 and 6, while the NEDTs are approximately one to two orders of magnitude smaller. Therefore, the NOAA-20 LC coefficients trained for one satellite are still applicable and perform well for both SNPP and NOAA-21.

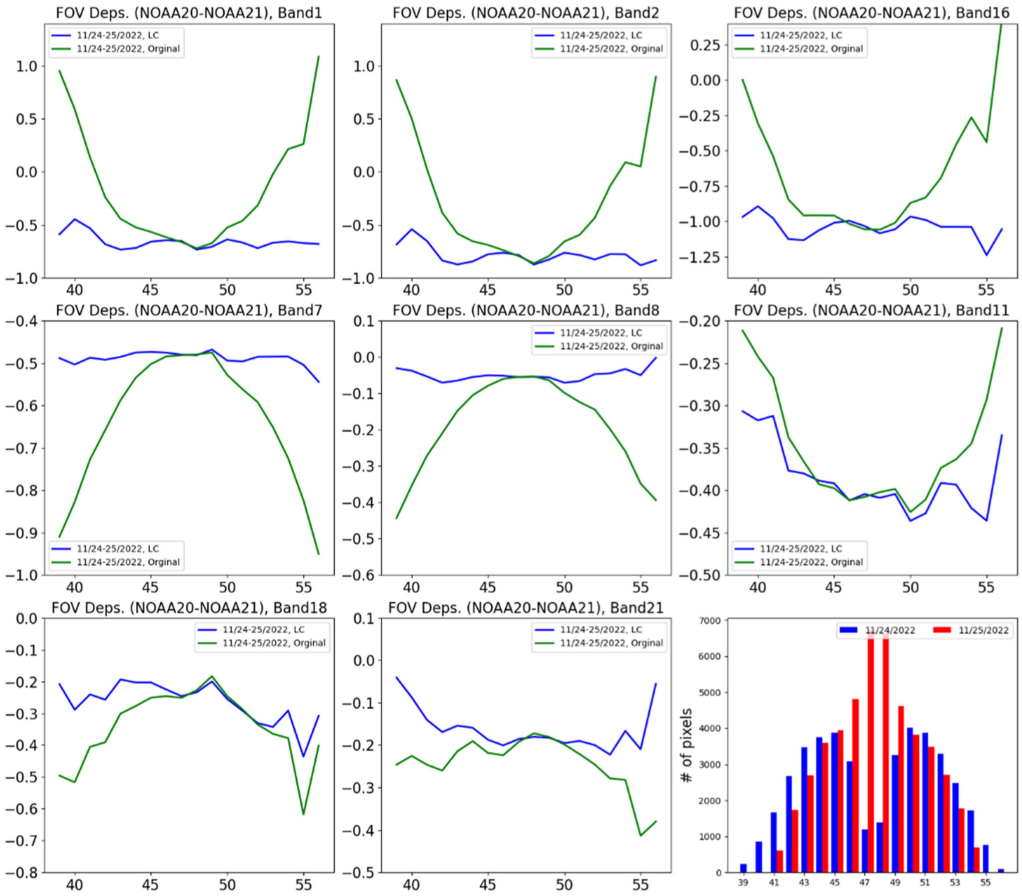

Fig. 5. Different BTs of ATMS paired pixels between NOAA-20 LC adjustment and NOAA-21 nadir as a function of FOV position and corresponding the distribution of number of pixels.

D. Combined LC and RE for Visualization Enhancement of Extreme Weather Events

The limb-adjusted BTs were input to the RE module to enhance image resolution by a factor of four. One objective of RE module is to clearly identify extreme weather events, such as TCs.

The ATMS channel 16 (88.2 GHz) and 17 (165.5 GHz) are two high-frequency window channels with over twice the resolution of channel 1 and 2. The features associated with the TCs become more distinct in these channels. Channels 18–19 (183 GHz) are water vapor channels that have an even higher resolution than window channels and are sensitive to lower tropospheric humidity. Both channel groups are suitable for capturing weather events near the surface. Fig. 7 shows an extreme weather event captured by the NOAA-21 ATMS channel 16 and channel 18 on November 27, 2022, located over the North Atlantic Ocean near the North American coast. It is important to note that the color scale for channel 18 is opposite to channel 16 to better highlight the features in the extreme weather event. Top panels show the event using the original SDR BTs. The event captured by channel 16 was impacted by complex surface reflection, while the humidity sounding channel 18 showed a clearer representation of the weather event. After LC adjustment in the middle panels, the features in the weather event are more defined, particularly for the window channel 16. However, the resolution of the depiction of the event remains blurred, particularly for channel 16 at off-nadir locations, due to linear interpolation used to enhance image resolution. The bottom panels of Fig. 7 show that the resolution of the ATMS image was enhanced four-fold by the RE model. The event became much clearer after being enhanced by ESRGAN and retained more detailed textures. Fig. 8 further enlarges the subregion of the middle and bottom panels of Fig. 7 from (55°W, 25°N) to (50°W, 30°N), which is close to the end of the rainbands. It is observed that the rainbands in both LC images are blurred, but become finer in structure after RE processing, making the benefits of RE image clearer.

Fig. 9 depicts Hurricane Ian near Western Cuba and south of Florida, captured by NOAA-20 ATMS channel 17 on September 26, 2022, and channel 19 of S-NPP ATMS on September 27, 2022. The pattern of the hurricane appears similar to Fig. 7. The images after LC and RE processing provide a clearer depiction of hurricane eye and rainbands compared to the original images.

Overall, these initial results suggest that limb-corrected and ESRGAN-enhanced images provide a clearer and more detailed representation compared to the raw ATMS SDR images.

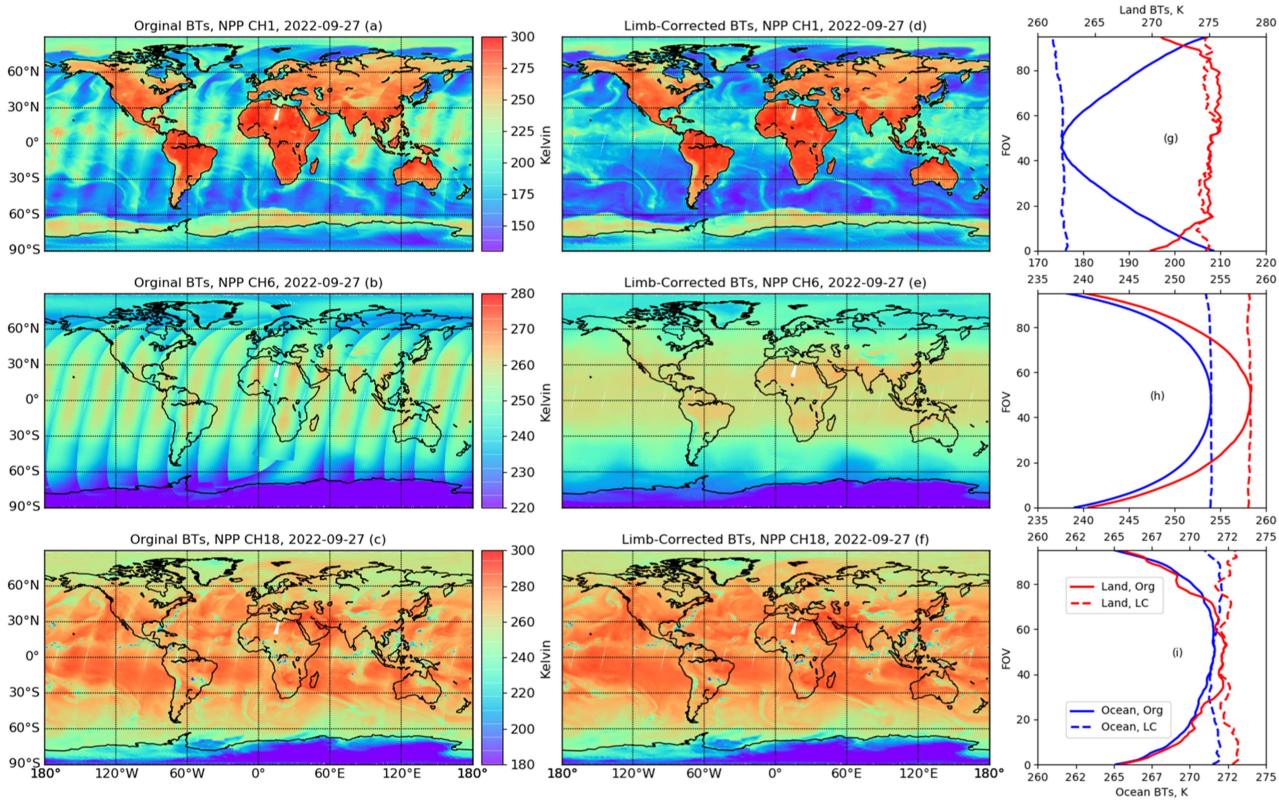

Fig. 6. Same as Fig. 3, but for S-NPP.

E. Preliminary Evaluation of RE BT Accuracy

Although the previous subsection demonstrated that the RE BT could improve the image visualization, the accuracy of the generated RE BT still needs to be quantitatively verified for its application in EDR products. Currently, no HR ATMS images are available to verify the RE model. However, a comparison between ATMS BTs and AMSR2 [33] onboard the Global Change Observation Mission-W1 satellite can be used to check the accuracy of the BT after RE, as the AMSR2 provides a channel at 89.0 GHz, similar to ATMS channel 16 (88.2 GHz), but with a higher spatial resolution of 5 km.

Unlike the cross-track scanning of ATMS, AMSR2 has a conical scan mechanism, with a fixed incidence angle of 55° at Earth surface, corresponding to a scan angle of 47° for channel 89.0 GHz. As a result, only the BTs at a 47° scan angle for ATMS channel 16 can be used for comparison with the AMSR2 channel at 89.0 GHz. In addition, AMSR2 measures both vertically and horizontally polarized BTs, while ATMS measures combined quasivertically polarized BTs. To compare the ATMS with AMSR2 BTs, the quasivertically polarized AMSR2 BTs (cBT) need to be calculated from their vertically and horizontally polarized BTs using the following formula:

$$\text{cBT} = \text{vBT} * \cos^2(\theta) + \text{hBT} * \sin^2(\theta) \tag{8}$$

where vBT and hBT are horizontally and vertically polarized measurements from AMSR2, respectively, and θ is the scan angle of AMSR2, which is constant at 47.0° for channel 89.0 GHz. As the AMSR2 BTs are not limb corrected, only the original SDR and RE BTs can be used for comparison, not limb-corrected BTs.

Fig. 10 displays RE image during the extreme weather event on November 27, 2022 and the corresponding AMSR2 image. Although the AMSR2 swath is narrower than ATMS and there are large gaps between the two adjacent orbits, the comparison is not significantly affected, as only the ATMS BTs at the 55° SZA are considered. This corresponds solely to the FOV scan positions of 5 and 89 in ATMS swath. To remove the effect of clouds, an approximate cloud detection algorithm, similar to the one used in the NOAA operational Integrated Calibration/Validation System (https://www.star.nesdis.noaa.gov/icvs/) was applied using ATMS SDR BTs for channels 1 and 2 [34]. Note that including cloudy and precipitating regions in the analysis may be better to identify the active extreme weather, as the RE method is most valuable in these conditions. However, it may introduce more noises and make quantitative analysis unstable. The collocation was performed under the rough assumption that the ATMS pixel size at a certain SZA is equivalent to the size at nadir, divided by the cosine of the SZA. This results in an approximate size of 56 km at 55° SZA for channel 16. Consequently, each ATMS pixel was paired with multiple AMSR2 pixels within a distance constraint of 56 km. For the RE ATMS pixel, this distance constraint was reduced to 14 km. The mean of the AMSR BTs for each pair was calculated and used for comparison with the corresponding ATMS BT. After collocating the ATMS and AMSR2 data, cloud screening, and removing 2σ

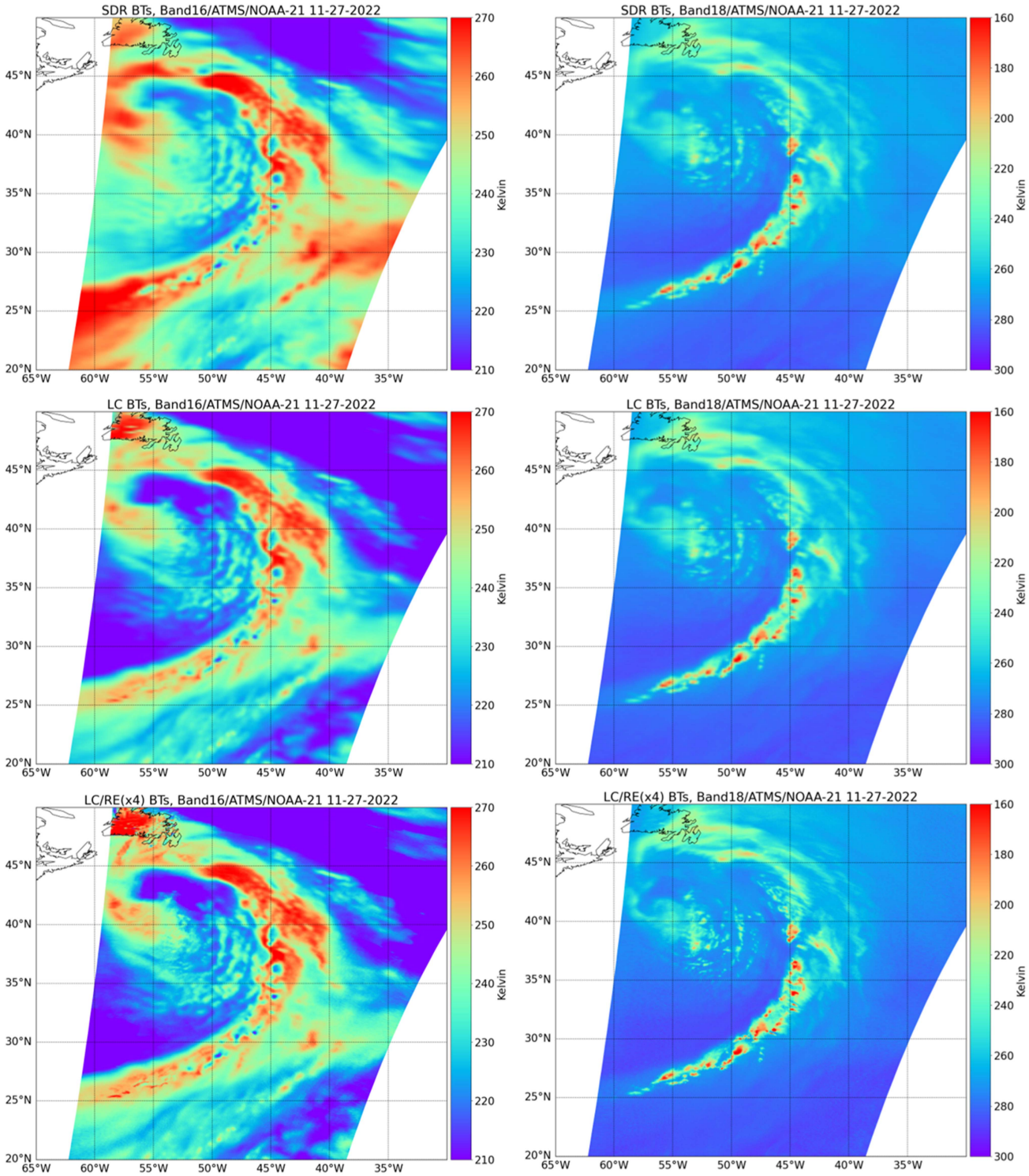

Fig. 7. Extreme weather event captured by NOAA-21 ATMS channel 16 (Left) and channel 18 (right) over the North Atlantic Ocean on 11/27/2022. Upper: SDR BTs; middle: LC BTs; and bottom: LC and RE BTs.

(SD) outliers, 396 ATMS-AMSR2 pair pixels were collected before RE and 6282 after RE. The data matchup was not subject to a time window constraint, with the exception of selecting only descending orbits for both sensors. These rough assumptions made during the collocation could introduce biases, particularly in the region of extreme weather events and variable surface states. While a more detailed analysis with accurate collocation and a large number of cases is necessary for the precise accuracy at the pixel level, the preliminary analysis may be considered acceptable for the imagery visualization objectives for this article.

The upper panels of Fig. 11 display the global distribution and scatter plot between ATMS SDR BTs and AMSR2 BTs. The lower panels compare the RE BTs with AMSR2. It was observed that a significant number of pair pixels at FOV position

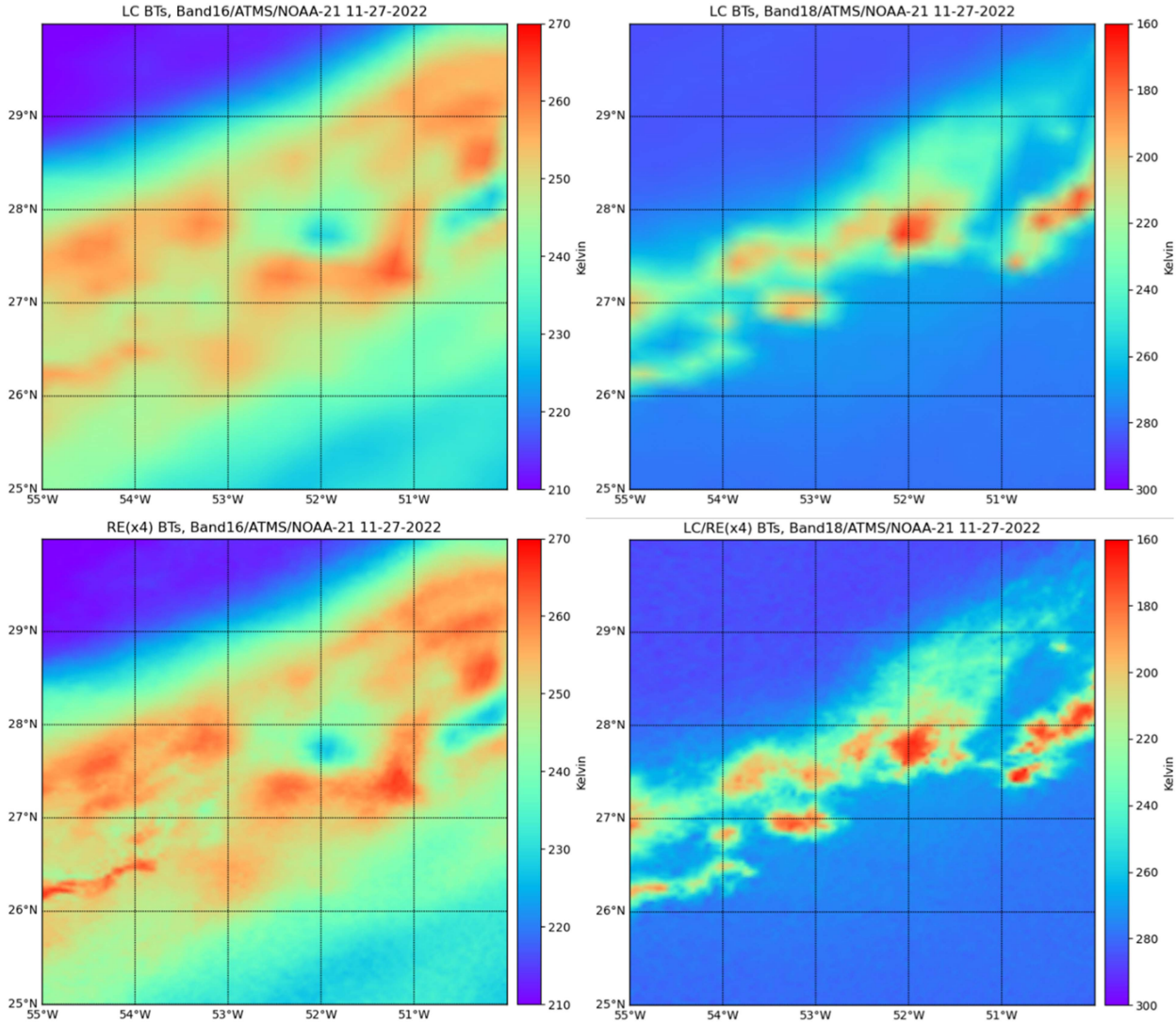

Fig. 8. Same as the middle and bottom panels of Fig. 6, but for subregion from (55°W, 25°N) to (50°W, 30°N).

89 (data close to 55°W longitude) were missing due to the gaps in the AMSR2 data and the region close to the weather event, where some pair pixels were removed by cloud screen algorithm. However, FOV position 5 (data between 30°W and 45°W) had all pair pixels. It is also found that larger biases and noises between ATMS BTs and AMSR2 BTs exist at position 89, partly due to the region's proximity to the weather event. The mean biases between RE BTs and AMSR2 BTs were found to be 0.038 K, smaller than those obtained before the RE (−0.92 K). The SDs for both cases were slightly large (around 3.9 K), which may be partly due to AMSR2 Level 1B used in this comparison. The Level 1R product [33] corrected BT in sensor footprint size, maybe suppressing some noise compared to Level 1B. However, both correlation coefficients were high (around 0.98), indicating a strong correlation between ATMS and AMSR2 BTs, particularly in regions with intense atmospheric changes.

This preliminary quantitative analysis might require further investigation and detailed evaluation. For instance, the application of LC and RE ATMS data in the retrieval of total precipitation water over ocean [6], or in the assessment of warm core parameters of TC [35], could offer additional insights into the model's accuracy when compared to the original ATMS SDR. Nonetheless, after RE processing, the image becomes clearer, while the mean biases between RE BTs and AMSR2 BTs were reduced, and both SDs and correlation confidences either decreased or remained similar. This further supports the effectiveness of the RE algorithm for ATMS data.

F. Full-Global LC RE Images in JSTAR Mapper

In anticipation of the upcoming weather season, and with the objective of rapidly identifying and analyzing TCs on a global scale, a test version of ATMS LC RE images is consistently being produced. These images cover the full globe and are plotted in an HR (9600 dpi × 4800 dpi) format for channels 6, 16, and 18. They are showcased on NOAA's internal JSTAR Mapper website, a web-based tool for visualizing NOAA satellite data. The generated near-real-time HR global images facilitate the

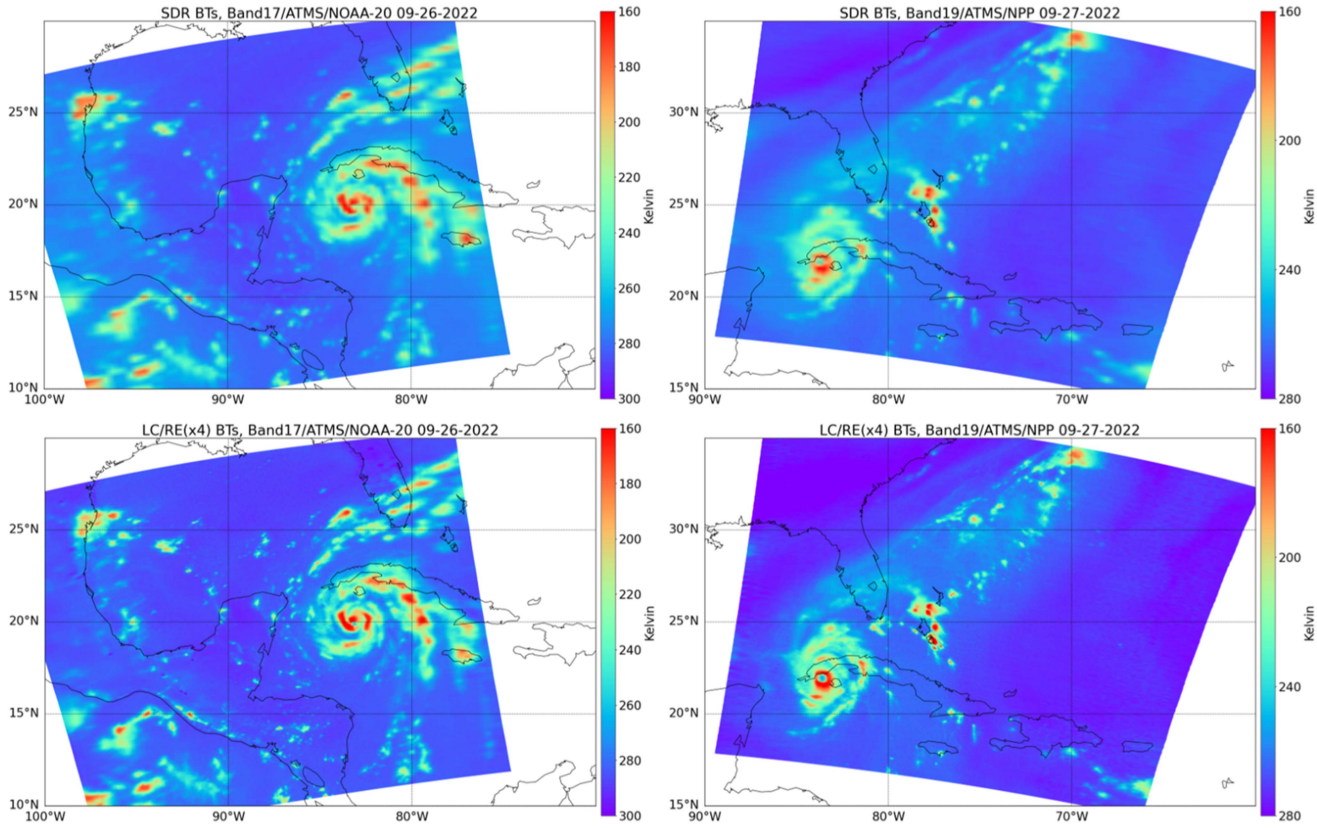

Fig. 9. Hurricane Ian observed in ATMS channel 17 on NOAA-20 (09/26/2022, left panels) and channel 19 on S-NPP (09/27/2022, right panels). (Upper) ATMS SDR; (lower) with LC and RE adjustment.

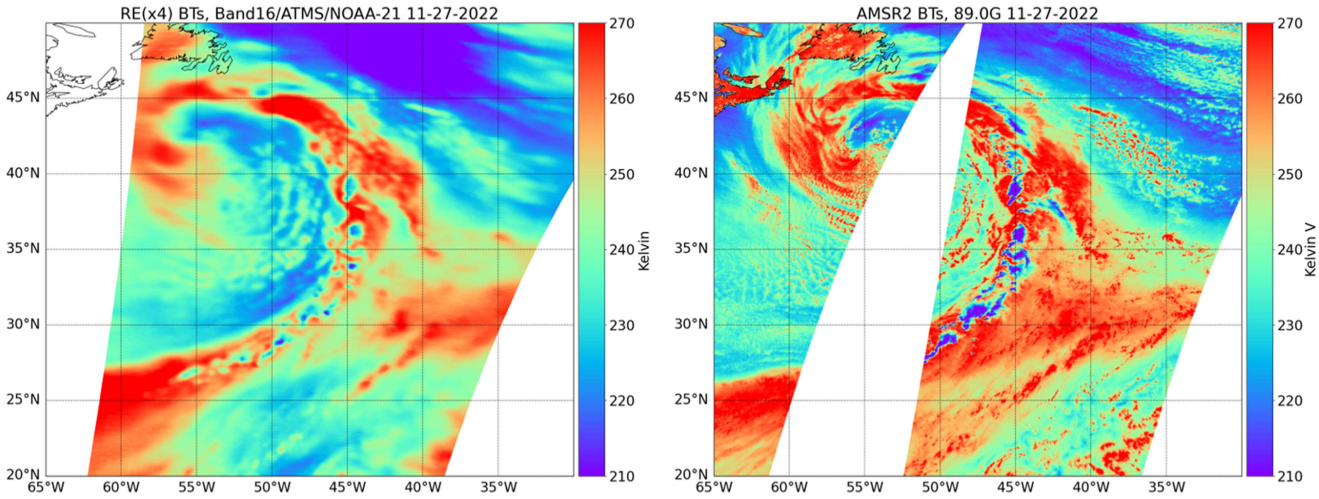

Fig. 10. RE NOAA-21 ATMS image for channel 16 (left) and AMSR2 image for 89.0 GHz (right) in 11/27/2022.

monitoring of ATMS SDR product and specific events like TCs, providing a detailed view both globally and regionally. Notably, these HR ATMS images are overlaid with true-color images from another essential JPSS sensor, the visible infrared imaging radiometer suite (VIIRS), in the visible bands. This combination enables users to distinguish possible precipitation from the dense cloud area surrounding the warm core of the TC.

Fig. 12 presents a global LC RE image on JSTAR Mapper from May 31, 2023 for ATMS water vapor sounding—channel 18, overlaid with the VIIRS true-color images. It highlights Typhoon "Mawar" in the vicinity of Taiwan (Box a). The intricacies of the event become more pronounced when zooming in on this specific region (Box b). Upon reducing the opacity of the ATMS image, it becomes evident that the typhoon's structure is congruent with the VIIRS true-color image (Box c). Such

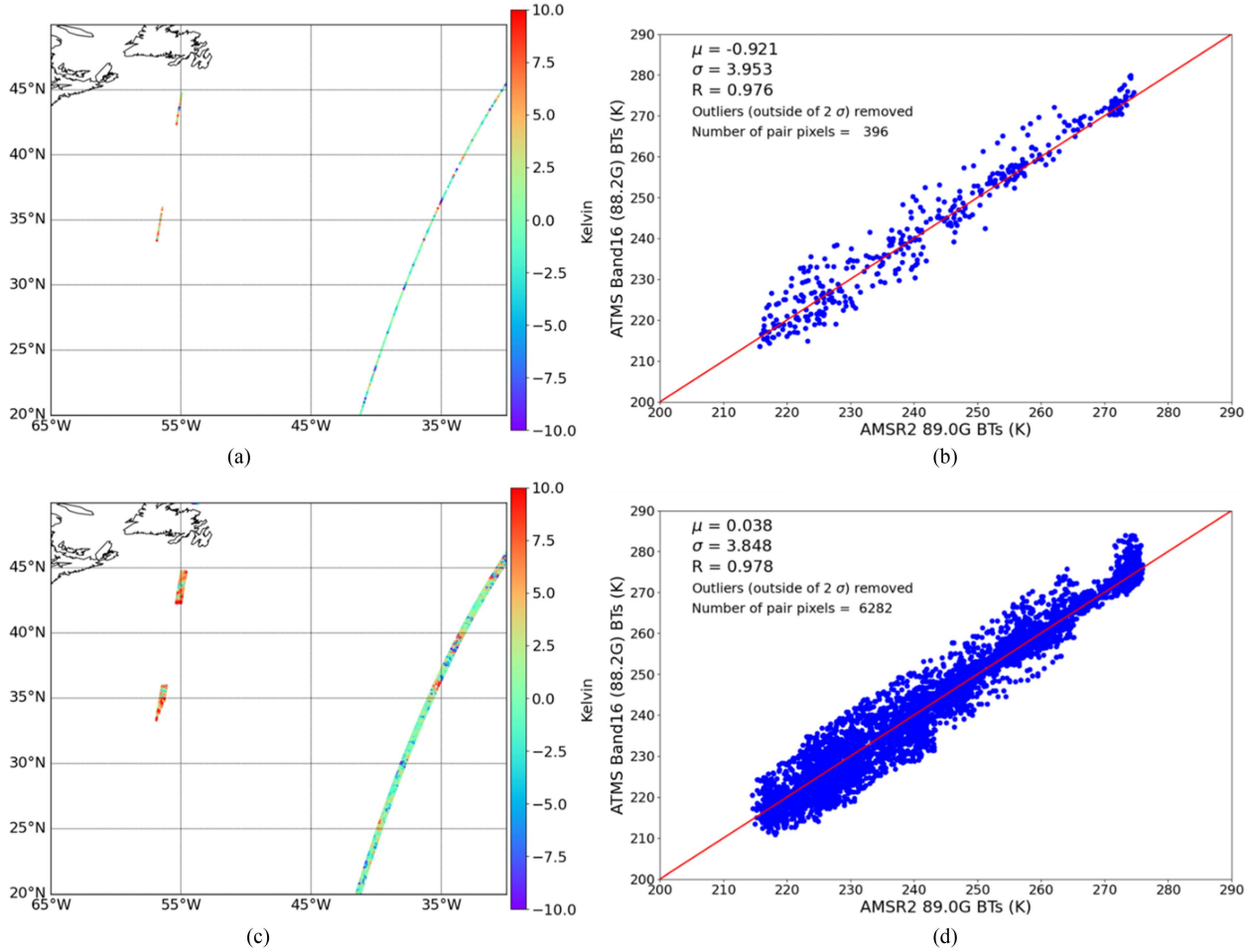

Fig. 11. Distribution of the ATMS-AMSR2 BT differences (a), (c) and corresponding scatter plots (b), (d) between ATMS BTs and AMSR2 BTs. (a), (b) Before ATMS RE. (c), (d) After ATMS RE.

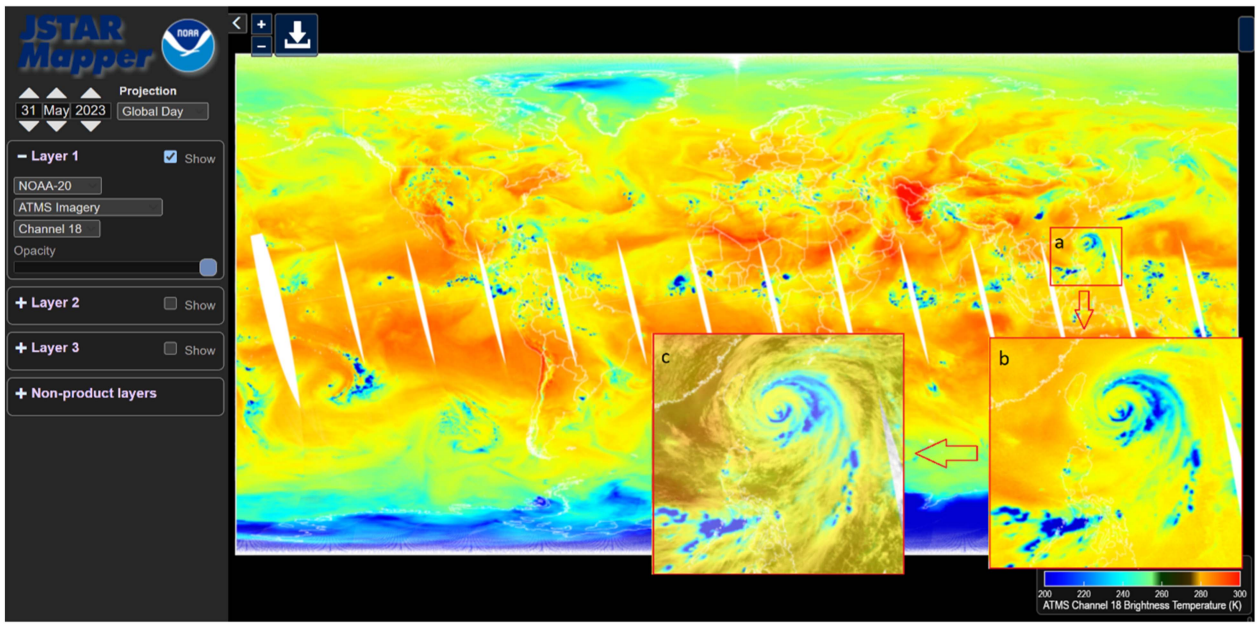

Fig. 12. Full-global LC RE Image in JSTAR mapper.

alignment allows for clear visualization of the warm core and the rainbands, details that may not be provided by the VIIRS visible image alone. Therefore, the combination of the ATMS LC RE image and VIIRS visible true-color image on the JSTAR Mapper provides a more comprehensive view of weather events.

Currently, significant efforts are underway to enhance ATMS LC RE images, steering them toward to an official release.

IV. Benefits and Limitations of Applying RE Model in ATMS

The RE model, also known as the ESRGAN model in this article, generally works well for the ATMS data for several window and near-surface temperature and humility sounding channels. However, it has certain limitations when it comes to all ATMS channels.

First, the RE model is limited by its lack of specific remote sensing and atmospheric information. This makes the RE unsuitable to predict realistic and detailed textures for very LR window channels in ATMS, which are affected by complex surface states and near-surface atmospheric changes. When the RE model was tested on channel 1 and 2, the RE images were showed minimal improvement, and in some areas, additional noise was observed. Second, the RE model does not take into account the different size of sensor footprint from nadir to off-nadir. In cross-track ATMS sensors, the footprint size at swath end is 3–4 times larger than that at nadir, which means that the RE model may not be able to fully capture the details in these larger footprints. All limitations require additional surface and atmosphere information to be resolved and improved, such as surface emissivity, wind speed, or atmosphere profiles, maybe including fine simulations from radiative transfer models, which is so-called integrating physical model in DL [36], [37]. This highlights the need for future article to further improve the RE model by finding the HR image used as reference in the model and incorporating remote sensing and atmospheric information into the training data.

In addition, the imagery for the higher peaking temperature sounding channels were not discussed here as these channels are not as effective in showing surface state and near-surface atmospheric changes as channel 16 and near-surface sounding channels.

Despite some limitations in RE application in ATMS windows channels, the RE model generally works well for most of humidity sounding channels, and in some cases for the window channels and low-peak temperature sounding channels, such as channel 6 and 16, as were discussed in the last section. For the current situation where HR images are lacking, ESRGAN is still deemed to be a suitable method to quickly and directly provide multichannel RE images, which is an effective method to improve ATMS imagery together with LC methods to assist in the identification of surface states and extreme weather events. Moreover, the RE model can be easily expanded to visible and infrared sensors, or other microwave sensors, to improve sensor imagery visualization. as the model itself and trained data are not dependent on the specific sensor or channel.

V. Conclusion

A method combining LC and RE was developed to improve ATMS imagery for clearer visualization of surface and atmosphere information and accurate identification of extreme weather events. The LC coefficients were generated through linear regression with NOAA-20 ATMS SDR data. The RE model was trained using an HR image set—DIV2K, and the well-trained model was applied to enhance ATMS image resolution by a factor of four.

The generated LC coefficients were used to generate LC images for both NOAA-20 and S-NPP ATMS to assess the accuracy and compatibility of the LC method, and the generated NOAA-20 LC BTs were further evaluated using data from the recently launched NOAA-21 satellite during a time when its orbit was nearly coincident to NOAA-20. The RE model was used to generate LC and RE BTs for multichannels after LC adjustment, and the accuracy of RE BTs was further evaluated quantitatively using HR AMSR2 data.

After LC adjustments, the angle dependence between the differences of the original NOAA-20 BTs and NOAA-21 BTs was eliminated or reduced, and performing best for temperature sounding channels, followed by water vapor sounding and window channels. Applying NOAA-20 LC coefficients to generate LC BTs for S-NPP or NOAA-21 produced similar patterns in scan angle dependence, implying good compatibility of NOAA-20 LC algorithm.

Extreme weather event became much clearer after LC adjustment and being enhanced by ESRGAN, retaining more detailed textures for channels 16–19 for S-NPP, NOAA-20, and NOAA-21. These qualitative analyses suggest that the LC and RE models are effective for most of ATMS water vapor sounding channels and window channel 16. The RE BTs for NOAA-21 were further initially and quantitatively evaluated using 5-km resolution AMSR2 data in channel at 89.0 GHz, which is the similar ATMS channel 16. After careful comparison between ATMS and AMSR2, we found that the mean biases for RE BTs minus AMSR2 BTs were smaller than those for the original SDR BTs minus AMSR2 BTs, and corresponding SDs and correlation confidences are comparable. While this quantitative analysis may require further investigation, the initial findings support the effectiveness of the RE algorithm when applied to ATMS data. It also encourages continued exploration of the accuracy and the LC and RE model, which can assist in improving ATMS image virtualization. As of this writing, the generation of global ATMS LC and RE imagery is routinely processed and tested in the NOAA internal HR imagery visualization system—JSTAR Mapper, to quickly identify and analyze TCs in the upcoming weather season. Concurrently, ongoing efforts are underway for an official release.

Overall, combining the LC and RE methods greatly improves the image visualization, including surface and atmosphere information, and enables clear identification of extreme weather events. Future article will involve improving the RE model by finding the HR image to use as reference in the model, such as radiative transfer model simulations or AMSR2 images, which will allow for the incorporation of remote sensing and atmospheric information into the training data.

ACKNOWLEDGMENT

The manuscript contents are solely the opinions of the authors and do not constitute a statement of policy, decision, or position on behalf of NOAA or the U.S. government.

REFERENCES

[1] F. Weng et al., "Calibration of Suomi national polar-orbiting partnership advanced technology microwave sounder," *J. Geophys. Res.: Atmos.*, vol. 118, no. 19, pp. 11,187–11,200, 2013.
[2] H. Yang, F. Weng, and K. Anderson, "Estimation of ATMS antenna emission from cold space observations," *IEEE Trans. Geosci. Remote Sens.*, vol. 54, no. 8, pp. 4479–4487, Aug. 2016.
[3] D. Q. Wark, "Adjustment of TIROS operational vertical sounder data to a vertical view," NOAA Tech. Rep. NESDIS-64, vol. 36, 1993.
[4] M. Goldberg, D. Crosby, S. David, and L. Zhou, "The limb adjustment of AMSU-A observations: Methodology and validation," *J. Appl. Meteorol. Climatol.*, vol. 40, pp. 70–83, 2001.
[5] Q. Liu and F. Weng, "Uses of NOAA-16 and-18 satellite measurements for verifying the limb-correction algorithm," *J. Appl. Meteorol. Climatol.*, vol. 46, no. 4, pp. 544–548, 2007.
[6] K. Zhang et al., "A methodology to adjust ATMS observations for limb effect and its applications," *J. Geophys. Res.: Atmos.*, vol. 122, no. 21, pp. 11–347, 2017.
[7] X. Tian, X. Zou, and S. Yang, "A limb correction method for the microwave temperature sounder 2 and its applications," *Adv. Atmos. Sci.*, vol. 35, pp. 1547–1552, 2018.
[8] B. Yan et al., "Gap filling of advanced technology microwave sounder data as applied to hurricane warm core animations," *Earth Space Sci.*, vol. 7, no. 12, 2020, Art. no. e2019EA000961.
[9] L. Zhou et al., "Observed atmospheric features for the 2022 Hunga Tonga volcanic eruption from joint polar satellite system science data products," *Atmosphere*, vol. 14, no. 2, 2023, Art. no. 263.
[10] H. Yang et al., "ATMS radiance data products' calibration and evaluation," *IEEE Trans. Geosci. Remote Sens.*, vol. 60, pp. 1–11, 2022, doi: 10.1109/TGRS.2021.3123576.
[11] Q. Yuan et al., "Deep learning in environmental remote sensing: Achievements and challenges," *Remote Sens. Environ.*, vol. 241, 2020, Art. no. 111716.
[12] X. Liang, Q. Liu, B. Yan, and N. Sun, "A deep learning trained clear-sky mask algorithm for VIIRS radiometric bias assessment," *Remote Sens.*, vol. 12, no. 1, 2019, Art. no. 78.
[13] X. Liang, K. Garrett, Q. Liu, E. S. Maddy, K. Ide, and S. Boukabara, "A deep-learning-based microwave radiative transfer emulator for data assimilation and remote sensing," *IEEE J. Sel. Topics Appl. Earth Observ. Remote Sens.*, vol. 15, pp. 8819–8833, 2022, doi: 10.1109/JSTARS.2022.3210491.
[14] X. Liang and Q. Liu, "Applying deep learning to clear-sky radiance simulation for VIIRS with community radiative transfer model—Part 2: Model architecture and assessment," *Remote Sens.*, vol. 12, no. 22, 2020, Art. no. 3825.
[15] X. Liang and Q. Liu, "Applying deep learning to clear-sky radiance simulation for VIIRS with community radiative transfer model—Part 1: Develop AI-based clear-sky mask," *Remote Sens.*, vol. 13, no. 2, 2021, Art. no. 222.
[16] L. Ma, Y. Liu, X. Zhang, Y. Ye, G. Yin, and B. A. Johnson, "Deep learning in remote sensing applications: A meta-analysis and review," *Int. Soc. Photogrammetry Remote Sens. J. Photogrammetry Remote Sens.*, vol. 152, pp. 166–177, Jun. 2019.
[17] I. Goodfellow et al., "Generative adversarial nets," in *Proc. Int. Conf. Neural Inf. Process. Syst.*, 2014, pp. 2672–2680.
[18] A. Creswell, T. White, V. Dumoulin, K. Arulkumaran, B. Sengupta, and A. A. Bharath, "Generative adversarial networks: An overview," *IEEE Signal Process. Mag.*, vol. 35, no. 1, pp. 53–65, Jan. 2018.
[19] K. O'Shea and R. Nash, "An introduction to convolutional neural networks," 2015, *arXiv:1511.08458*.
[20] Y. Li and M. Momen, "Detection of weather events in optical satellite data using deep convolutional neural networks," *Remote Sens. Lett.*, vol. 12, no. 12, pp. 1227–1237, 2021.
[21] A. Chattopadhyay, P. Hassanzadeh, and S. Pasha, "Predicting clustered weather patterns: A test case for applications of convolutional neural networks to spatio-temporal climate data," *Sci. Rep.*, vol. 10, 2020, Art. no. 1317.
[22] M. Toğaçar, B. Ergen, and Z. Cömert, "Detection of weather images by using spiking neural networks of deep learning models," *Neural Comput. Appl.*, vol. 33, pp. 6147–6159, 2021.
[23] Z. Zhang, H. Wang, F. Xu, and Y.-Q. Jin, "Complex-valued convolutional neural network and its application in polarimetric SAR image classification," *IEEE Trans. Geosci. Remote Sens.*, vol. 55, no. 12, pp. 7177–7188, Dec. 2017.
[24] S. Chen, H. Wang, F. Xu, and Y.-Q. Jin, "Target classification using the deep convolutional networks for SAR images," *IEEE Trans. Geosci. Remote Sens.*, vol. 54, no. 8, pp. 4806–4817, Aug. 2016.
[25] C. E. Duchon, "Lanczos filtering in one and two dimensions," *J. Appl. Meteorol. Climatol.*, vol. 18, no. 8, pp. 1016–1022, 1979.
[26] C. Dong, C. C. Loy, K. He, and X. Tang, "Image super-resolution using deep convolutional networks," *IEEE Trans. Pattern Anal. Mach. Intell.*, vol. 38, no. 2, pp. 295–307, Feb. 2016.
[27] J. Kim, J. K. Lee, and K. M. Lee, "Accurate image super-resolution using very deep convolutional networks," *IEEE Conf. Comput. Vis. Pattern Recogn.*, Las Vegas, NV, USA, 2016, pp. 1646–1654, doi: 10.1109/CVPR.2016.182.
[28] C. Ledig et al., "Photo-realistic single image super-resolution using a generative adversarial network," in *Proc. IEEE Conf. Comput. Vis. Pattern Recognit.*, 2017, pp. 4681–4690.
[29] X. Wang et al., "ESRGAN: Enhanced super-resolution generative adversarial networks," in *Proc. Eur. Conf. Comput. Vis. Workshops*, 2018.
[30] A. Jolicoeur-Martineau, "The relativistic discriminator: A key element missing from standard GAN," 2018, *arXiv:1807.00734*.
[31] K. Simonyan and A. Zisserman, "Very deep convolutional networks for large-scale image recognition," in *Proc. Int. Conf. Learn. Representations*, 2015.
[32] E. Agustsson and R. Timofte, "NTIRE 2017 challenge on single image super-resolution: Dataset and study," in *Proc. IEEE Conf. Comput. Vis. Pattern Recogn. Workshops*, Honolulu, HI, USA, 2017, pp. 1122–1131, doi: 10.1109/CVPRW.2017.150.
[33] T. Maeda, Y. Taniguchi, and K. Imaoka, "GCOM-W1 AMSR2 level 1R product: Dataset of brightness temperature modified using the antenna pattern matching technique," *IEEE Trans. Geosci. Remote Sens.*, vol. 54, no. 2, pp. 770–782, Feb. 2016.
[34] F. Weng, L. Zhao, R. R. Ferraro, G. Poe, X. Li, and N. Grody, "Advanced microwave sounding unit cloud and precipitation algorithms," *Radio Sci.*, vol. 38, pp. 33–31, 2003.
[35] T. Zhu and F. Weng, "Hurricane sandy warm-core structure observed from advanced technology microwave sounder: ATMS-derived tropical cyclone warm cores," *Geophys. Res. Lett.*, vol. 40, pp. 3325–3330, 2013.
[36] G. Dong, W. Huang, W. A. P. Smith, and P. Ren, "A shadow constrained conditional generative adversarial net for SRTM data restoration," *Remote Sens. Environ.*, vol. 237, 2020, Art. no. 111602.
[37] C. Wang, E. Bentivegna, W. Zhou, L. Klein, and B. Elmegreen, "Physics-informed neural network super resolution for advection-diffusion models," *Neural Inf. Process. Syst.*, vol. 2020, 2020.

Xingming Liang received the Ph.D. degree in remote sensing from the Saga University, Saga, Japan, in 2005.

He is currently an Associate Research Scientist with the Cooperative Institute for Satellite Earth System Studies (CISESS), University of Maryland (UMD), College Park, MD, USA. He subsequently served as a Postdoctoral Researcher with the Institute of Ocean Energy Saga University until 2007. From 2007 to 2016, he worked as a Research Scientist with the Cooperative Institute for Research in the Atmosphere, Colorado State University, Fort Collins, CO, USA, and developed the NOAA leading sea surface temperature (SST) product—Advanced Clear-Sky Processor over Ocean and SST real-time monitoring system—Monitoring of Infrared Clear-sky Radiance over Ocean for SST in collaboration with the NOAA Center for Satellite Applications and Research SST team. From 2016 to 2019, he served as a Senior Scientist with the Earth Resources Technology Inc., where he supported VIIRS calibration and validation and NOAA Integrated Calibration and Validation System system. Since 2019, he has been working with the CISESS, UMD, focusing on ATMS calibration and validation, artificial intelligence applications in remote sensing, data assimilation, and radiative transfer model.

Lihang Zhou received the M.S. degree in meteorology from the University of Maryland, College Park, in 1993.

She worked as a Senior Data Product and an Algorithm Scientist with the NOAA Integrated Program Office, Lanham, MD, USA, from 2009 to 2011, then as the Satellite Applications and Research (STAR) JPSS Program Manager with the NOAA/STAR until 2019, and the Science Deputy for the JPSS Algorithm Management Project. She is currently the Data Products Management and Services Deputy and the Products Portfolio Manager with the National Oceanic and Atmospheric Administration Joint Polar Satellite System, Lanham. She has extensive experience in the fields of satellite algorithm development, calibration/validation, and program management.

Ms. Zhou was a member of the National Aeronautics and Space Administration Atmospheric IR Sounder Sounder Science Team from 2002 to 2006, working on algorithm development for retrieving products from hyperspectral infrared sounding instruments and then becoming the QA manager on the GOES-R algorithm working group from 2006 to 2009.

Mitch Goldberg received the B.S. degree from Rutgers University, New Brunswick, NJ, USA, and the M.S. and Ph.D. degrees from the University of Maryland, College Park, MD, USA.

He is currently a Distinguished Research Professor with the NOAA Center for Earth System Sciences and Remote Sensing Technologies (CESSRST), City College of New York, New York, NY, USA. He retired from NOAA after 35 years in May 2023, and his last appointment at NOAA was serving as the NOAA-NESDIS Chief Scientist. At NOAA, he was an expert and lead representative of the NOAA-NESDIS science and user communities and coordinated NESDIS applied science within NOAA and with partner federal and international agencies. His scientific expertise is in developing scientific algorithms to derive atmospheric soundings of temperature and water vapor from satellite platform microwave and infrared sounders.

Dr. Goldberg is a Fellow of the American Meteorological Society (AMS), and the Chair Emeritus of the AMS Satellite Meteorological, Oceanography, and Climatology Committee. He was the recipient of three Gold Medals, one Silver Medal, and ten Bronze Medals from the Department of Commerce including the 2010 NOAA Administrator's Award for leadership in developing the international Global Space-based Inter-Calibration System (GSICS) and the University of Maryland Most Distinguished Alumnus Award from the Department of Atmospheric and Oceanic Science in 2004.

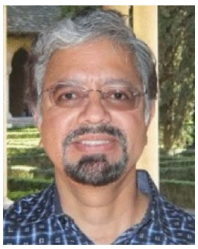

Satya Kalluri received the M.Sc. degree in geography from the Osmania University, Hyderabad, India, in 1990, and the Ph.D. degree in geography from the University of Maryland College Park, College Park, MD, USA, in 1994.

He is currently the Program Scientist for the JPSS and LEO Program with the NOAA NESDIS, College Park, MD, USA, and provides independent advice to the Program Director on sensor science and applications as well as overseeing the proving ground and risk reduction activities. He has more than 25 years of experience in the formulation, management, and development of several remote sensing missions. Prior to joining JPSS, he was a Division Chief with the NESIDS Center for Satellite Applications and Research (STAR). While working with the STAR, he saw the development of algorithms and products to process remote sensing data from a variety of LEO and GEO satellite missions for NOAA and non-NOAA users in land and atmosphere applications. He led the development of the product generation and distribution segment of the GOES-R ground system with NOAA. Before joining NOAA, he was with the Aerospace Corporation, Raytheon and the University of Maryland at College Park on several remote sensing projects. His research interests include land and atmosphere remote sensing.

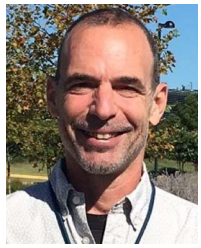

Christopher Grassotti received the B.S. degree in Earth and space science from the State University of New York, Stony Brook, NY, USA, in 1982, the M.S. degree in meteorology from the University of Wisconsin-Madison, Madison, WI, USA, in 1986, and the M.S. degree in viticulture and enology from the AgroMontpellier, Montpellier, France, in 2007.

From 1986 to 1991 and again from 1993 to 2005, he was a Research Associate and a Senior Research Associate with the Atmospheric and Environmental Research, Inc., Lexington, MA, USA. From 1991 to 1993, he worked with the Atmospheric Environmental Service, Environment Canada, Dorval, QC, Canada. Since 2008, he has worked with the National Oceanic and Atmospheric Administration, NOAA Center for Satellite Application and Research, National Environmental Satellite, Data, and Information Service, College Park, MD, USA, and is currently a Senior Faculty Specialist with the Earth System Science Interdisciplinary Center, and with the University of Maryland, College Park, MD, USA.

Ninghai Sun received the Ph.D. degree in atmospheric remote sensing from the University of Maryland, College Park, MD, USA, in 2009.

Since 2002, he has worked with the Center for Satellite Application and Research, National Oceanic and Atmospheric Administration (NOAA) as a Senior Project Engineer/Scientist. He is currently the Technical Lead of the JPSS Advanced Technology Microwave Sounder (ATMS) calibration/validation team. He is also the creator of the STAR operational Integrated Cal/Val System, which is a real time on-orbit instrument status/performance and science data quality monitoring system for NOAA, NASA, and EUMETSAT operational meteorological weather satellites to support NOAA critical missions. He is also the Principle Engineer to develop the JPSS lifecycle reprocessing system for ATMS, CrIS, and OMPS to support the intersatellite calibration and data product long-term trending for climate study. His research interests include development of operational weather satellite microwave instrument calibration theory, the implementation of microwave instrument ground processing calibration algorithms, and the development of environmental product retrieval algorithms.

Banghua Yan received the Ph.D. degree in atmospheric physics from the Institute of Atmospheric Physics, Chinese Academy of Sciences, Beijing, China, in 1997, and the Ph.D. degree in atmospheric radiation from the University of Alaska, Fairbanks, USA, in 2001.

She is currently a Physical Scientist with the Satellite Calibration Branch, NOAA Center for Satellite Applications and Research (STAR). From 1999 to 2010, she worked with the STAR through scientific companies or NOAA Joint Center for Satellite Data Assimilation (JCSDA) or the Earth System Science Interdisciplinary Center, University of Maryland, College Park, MD, USA. During this period, she significantly contributed to the developments of microwave land, snow, and sea ice emissivity models, and microwave satellite instrument data assimilation studies. The land, snow, and sea ice microwave emissivity models have been implemented into the NOAA NCEP NWP model and the JCSDA community radiative transfer model that has been successfully used in several operational data assimilation systems in the U.S. From 2010 to 2017, she was an Oceanographer with the NOAA Office of Satellite Data Processing and Distribution, Camp Springs, MD, to lead the NOAA operational ocean color production system. She has authored/coauthored more than 30 papers in international peer-reviewed journals. In addition, from 2017 to 2019, she successfully led calibrations/validations of Metop-C Advanced Microwave Sounding Unit-A (AMSU-A) to ensure the operation of AMSU-A data. She also coordinated the JPSS/STAR mission program for more than half years. Currently, she leads calibrations/validations of Joint Polar Satellite System Ozone Mapping and Profiler Suite and the STAR Integrated Calibration/Validation System Long-Term Monitoring.

Hu Yang received the Ph.D. degree from the Institute of Remote Sensing Application, China Academy of Science, Beijing, China, in 2003.

He has more than 20 years of experience on active and passive microwave remote sensing, microwave radiometer ground and on-orbit calibration, satellite geolocation, and ground calibration processing system development. Since 2012, he has been with the Cooperative Institute for Satellite Earth System Studies, University of Maryland, College Park, MD, USA, where he is currently a Research Scientist, focusing on S-NPP and JPSS ATMS calibration/validation. He has authored more than 40 peer-reviewed journals on microwave remote sensing-related studies.

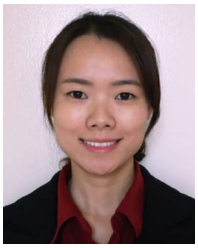

Lin Lin received the Ph.D. degree in meteorology from the Florida State University, Tallahassee, FL, USA, in 2009.

She is currently a General Engineer with the NOAA/NESDIS/Systems Architecture and Engineering. From 2011 to 2022, she worked with the NESDIS/Center for Satellite Applications and Research, focusing on the calibration, intercalibration, applications, and reprocessing of the instruments onboard the Suomi National Polar-orbiting Partnership, NOAA-20, and the following Joint Polar Satellite System satellites.

Dr. Lin is the recipient of the JPSS Internal "Unseen Heroes" Award and the NESDIS You Got Caught Award in 2022.

Quanhua Liu received the B.S. degree from the Nanjing University of Information Science and Technology (former Nanjing Institute of Meteorology), Nanjing, China, in 1982, the master's degree in physics from the Chinese Academy of Science, Beijing, China, in 1984, and the Ph.D. degree in meteorology and remote sensing from the University of Kiel, Kiel, Germany, in 1992.

He is currently a Physical Scientist with the NOAA/NESDIS Center for Satellite Applications and Research. He is leading the NOAA Microwave Integrated Retrieval System that retrieves 10 environmental data records. He is also working as a colead of the Community Radiative Transfer Model in the USA. His research interests include deep-learning algorithms, radiative transfer models, satellite products, and climate studies.